Virtual Friction: Experimental Validation in a Microgrid of 3 Virtual Synchronous Machines

Virtual Friction: Experimental Validation in a Microgrid of 3 Virtual Synchronous Machines

Florian Reissner Vincenzo Mallemaci Fabio Mandrile Radu Bojoi George Weiss

***Abstract*—Virtual synchronous machines (VSMs) are a promising technology to integrate distributed energy sources and storage into power grids. The VSM is a power converter that emulates the behavior of a synchronous machine, providing grid services which are necessary to operate a power system in a stable manner. When more VSMs are connected to the same grid, subsynchronous oscillations between them (and between VSMs and other generators) may occur if damping coefficients and inertias are not properly tuned. For this purpose, virtual friction (VF) has been proposed to provide high damping without a strong coupling of frequency deviation and power output, unlike for frequency droop. VF applies a damping torque to the virtual rotor of the VSMs, proportional to the deviation of the rotor frequency from the center of inertia (COI)-frequency of the grid. To the best of the authors' knowledge, this technique has only been validated theoretically and in simulations for isolated microgrids. The goal of this paper is to demonstrate the effectiveness of VF both in isolated microgrids and in grid connected operation by experiments on a 45kVA setup and their theoretical assessment.**

***Index Terms*—Virtual Synchronous Generator, Virtual Friction, Microgrid, Islanding, Frequency synchronization**

I. Introduction

A virtual synchronous machine (VSM) is an inverter controlled such that it emulates the behavior of a synchronous generator. It has become a popular technology to respond to stability requirements of electric grids with a large share of inverter-based power supply [1]–[9]. Since VSMs use digital control algorithms, they are inherently more flexible than synchronous generators (SGs) and open up new ways to improve grid stability and operation. One such idea is virtual friction (VF) [10], [11]. VF applies a damping torque to the swing equation of a VSM, which introduces damping proportional to the deviation of the virtual rotor frequency of the VSM from the center of inertia (COI)-frequency ω_{COI}: a weighted average of the frequencies of the (virtual) synchronous generators in the grid. In this way, VF leads to a much lower injection of excess power during drops of the grid frequency, when compared to classical frequency droop. This is beneficial especially for power plants where such a sudden increase in output power is not desirable or even impossible due to limitations of the primary energy source (e.g., solar or wind production). While VF has been shown to be an efficient way to damp oscillations between two areas of an isolated grid in simulations and through theoretical analysis [11], it remains to be demonstrated experimentally that VF can stabilize a microgrid of real inverters. Moreover, it is important to investigate the performance of VF, when such a microgrid is part of a larger grid where not all machines employ the VF mechanism. Based on the results in [11], we provide such an experimental validation in a microgrid consisting of three inverters operating in both islanded mode and grid-connected mode. We compare the system behavior when mainly VF is used with scenarios where similar damping was applied using frequency droop or high frequency (HF) droop. The remainder of this paper is structured as follows. In Sec. II we give a brief theoretical description of the VSMs and VF. In Sec. III we show our experimental setup and selected results obtained for the microgrid under consideration.

This research was co-funded by the European Union's Horizon 2020 research and innovation program under the Marie Sklodowska-Curie grant agreement no. 861398. V Mallemaci, F. Mandrile and R. Bojoi are with the Energy Department "Galileo Ferraris" (DENERG), Politecnico di Torino, 10129 Torino, Italy. F. Reissner and G. Weiss are with the School of Electrical Engineering, Tel Aviv University, Ramat Aviv 69978, Israel. (e-mail: reissner@tauex.tau.ac.il, vincenzo.mallemaci@polito.it, fabio.mandrile@polito.it, radu.bojoi@polito.it, george.weiss@tauex.tau.ac.il)

II. System description

The VSM algorithm used in these experiments is based on [12], [13]. We briefly reintroduce here the main features, mainly the swing equation, the reactive power control loop and the fast current controllers. In Fig. 1 a simplified block diagram of this VSM is given.

The torque equation of the VSM in [12], [13] is

$$J\omega = \int \mathscr{S}(T_d + T_m - T_e)dt, \tag{1}$$

where $\int \mathscr{S}$ is the saturating integrator explained below, J and ω are the VSMs inertia and frequency respectively, T_m is the mechanical torque, calculated from the active and reactive power set points, T_e is the electric torque and T_d is the damping torque, consisting of frequency droop and VF, as shown in Fig. 2. The saturating integrator behaves most of the time like a normal integrator, but forces the result of the integration to stay within a predetermined interval, see [12]–[14]. The rotor frequency from Eq. (1) is integrated (modulo 2π) to obtain the rotor angle θ, which is used for all Park transformations and to generate the synchronous internal voltages $e = [e_a \;\; e_b \;\; e_c]^\top$. These are calculated by

$$e = \sqrt{\frac{2}{3}}\omega m i_f \widetilde{\sin\theta},$$

where i_f is the field current in the electric rotor, $m = \sqrt{2/3}M_f, M_f > 0$ is the peak mutual inductance between the rotor winding and any one stator winding and $\widetilde{\sin\theta} = [\sin\theta \;\; \sin(\theta - \frac{2\pi}{3}) \;\; \sin(\theta + \frac{2\pi}{3})]^\top$. The difference between e and the measured grid voltage $v = [v_a \;\; v_b \;\; v_c]^\top$ is fed

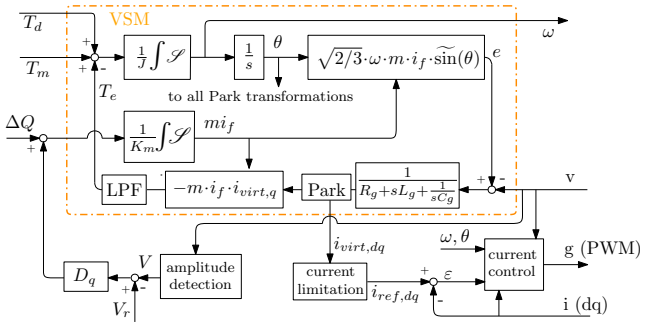

Figure 1: A simplified block diagram of the VSM from [13] showing the swing equation of the virtual rotor, the field current controller and the current controller that has the task to minimize the error ε between the current reference i_{ref} and the measured currents i_{dq}.

through a virtual impedance, a series connection of a resistive, inductive and capacitive part, R_g, L_g and C_g respectively. The output of this block gives the virtual currents i_{virt}, which are then Park transformed. The q component of the virtual currents is used to obtain the electric torque $\tilde{T}_e = -mi_f i_{virt,q}$, which, after low pass filtering by block LPF is fed back to Eq. (1).

Another saturating integrator is used in the reactive power controller to regulate the field current i_f, according to

$$mi_f = \frac{1}{K_m}\int \mathscr{S}(\Delta Q + D_q(V_r - V))dt,$$

where V_r is the reference voltage amplitude, V is the measured voltage amplitude, $D_q > 0$ is the voltage droop coefficient and $K_m > 0$ is a large constant. Furthermore, $\Delta Q = Q_{set} - Q$, where Q_{set} is the reference reactive power and Q is the measured reactive power output of the VSM.

Finally, a fast current controller is used to ensure that the measured grid currents follow the reference currents i_{ref}. These are obtained by passing $i_{virt,dq}$ through a current limitation block, to prevent overcurrents. The current controller receives ω, θ and the tracking error $\varepsilon = i_{ref,dq} - i_{dq}$ as inputs, and outputs the voltage references g for the PWM generation in abc-coordinates.

The (simplified) physical power circuit of phase a is shown in Fig. 3 (the other two phases are identical). The reference voltage g_a enters the PWM signal generator unit controlling the inverter leg of phase a, generating the output voltage signal $\tilde{g_a}$, whose average voltage over one switching cycle is g_a, or rather a slightly delayed g_a, due to processing delays and the PWM process. These are compensated by the current controller. The output voltage $\tilde{g_a}$ is filtered through an LCL filter, consisting of inductors L_s, L_2 and a capacitor C_s. The resistive parts of the coils are represented as R_s and R_2. In this setup, the grid voltage v_a is measured on the capacitor and the current i_a is measured on the inverter side.

The frequency droop is split into a low frequency (LF) and a HF component, such that the transfer functions of the first order low- and high-pass filters add up to 1.

In our realization, the filter time constant is 1s, and the HF-droop coefficient D_{HF} is usually 5 times larger than the LF-droop coefficient D_{LF}, such that HF components of the frequency deviation from its nominal value generate a stronger

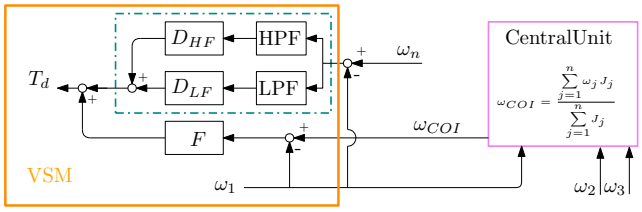

Figure 2: In a VSM with VF, the damping torque T_d is obtained by summing the VF and the HF and LF-droops. While the frequency droop torque is proportional to the difference between ω and the nominal frequency ω_n, the VF damping torque is proportional to the deviation of ω from ω_{COI}, the weighted average of all VSM frequencies (here ω_1, ω_2, ω_3).

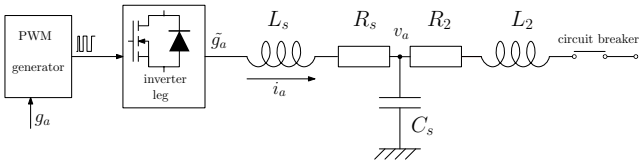

Figure 3: Phase a of the simplified power circuit of the inverter.

damping torque. Fig. 2 shows the block diagram for generating the damping torque T_d. The VF torque is proportional to $(\omega - \omega_{COI})$, where ω_{COI} (the weighted average of the generator frequencies) is calculated by a central controller. Note that, in case of an overall frequency drop in the grid, the difference $(\omega - \omega_{COI})$ only depends on the frequency differences in the grid. These differences can be kept small by sufficiently increasing the VF coefficient F (see [11]) such that in case of a large frequency drop, $(\omega - \omega_{COI})$ remains smaller than $(\omega - \omega_n)$. This allows to keep the active power output within reasonable bounds, while maintaining high damping.

For theoretical analysis, it is helpful to separate the system dynamics into three timescales: a very fast one, that models the dynamics of the current controller and the switches of the VSM (<1ms), a fast one, which models the dynamics of the virtual rotor (≈100ms) and a slow one which models secondary control (>10s). In the following analysis, we will neglect the dynamics of the secondary control. By ensuring good initial tuning and appropriate system impedances, we can assume that the current controllers are stable and that their dynamics can be regarded as static on the timescale of the fast system, which is the one of interest for us.

For the theoretical discussion of the power oscillations in a microgrid comprising three VSMs, we briefly introduce a simplified, but powerful model that is known to represent this type of dynamics well: the friction enhanced power system (FEPS) model [11]. This model is obtained from the network reduced power system (NRPS) model (see [15], [16] and Chapter 6 in [17]) by including VF. As the stability analysis of these models has been presented in the mentioned publications, we refrain from a detailed analysis. The FEPS model represents a power grid with n VSMs, connected via a passive network modeled by constant (complex) impedances. Each VSM is modeled as a constant amplitude, variable frequency, balanced three phase voltage source, generating positive sequence only. Under these assumptions, the FEPS model is given by the following n

equations. The swing equation for each VSM is:

$$M_j\ddot{\theta}_j + (F_j + D_j)\dot{\theta}_j = P_{set,j} + D_j\omega_n + F_j\omega_{COI} - P_{e,j},$$

where D_j is its frequency droop coefficient of VSM j, F_j is its VF coefficient and $P_{set,j}$ its set power. $M_j = \omega_n J_j$ where J_j is the inertia of the VSM. The electric power $P_{e,j}$ is dependent on the rotor angles θ_k of the VSMs:

$$P_{e,j} = \sum_{k=1}^{n} a_{jk} \sin(\theta_j - \theta_k - \varphi_{jk}),$$

where $a_{jk} = |Y_{jk}||E_j||E_k|$ for $1 \leq j,k \leq n$, with Y_{jk} being the line admittance between inverters j and k, $|E_j|$ is the amplitude of the output voltage of VSM j and $\tan\varphi_{jk} = \mathfrak{Re}(Y_{jk})/\mathfrak{Im}(Y_{jk})$. Note that unlike in [15], we have not put $a_{jj} = 0$. The center of inertia frequency ω_{COI} is defined as in [18]:

$$\omega_{COI} = \frac{\sum_{k=1}^{n} M_k\omega_k}{\sum_{k=1}^{n} M_k}.$$

HF-droop is not modeled in the NRPS model.

For simplicity, we introduce the following notation for the damping ratio and the fraction of VF of the overall damping:

$$\rho_j = \frac{D_j + F_j}{M_j}, \qquad \sigma_j = \frac{F_j}{D_j + F_j}, \qquad 1 \leq j \leq n.$$

Note that if HF droop is used, ρ_j is defined using the value of $D_{HF,j}$ instead of D_j, since system damping mainly depends on the HF droop. The parameters D_j, F_j and J_j can be used to adjust system dynamics for a given grid. Their influence on damping and frequency of the power oscillations can be understood by looking at a linearized version of the FEPS model.

We have linearized the FEPS model around the steady state of the (islanded) microgrid shown in Fig. 6 when using the line impedances, loads and set powers as defined in Sec. III-A and when L_2 is disconnected. Fig. 4 shows pole maps of the system with lines of constant inertia J, damping D and damping ratio ρ in grey. While ρ in this system was the same for each VSM, the values of D and J noted on the lines in the figure must be multiplied with $[0.6\ \ 0.4\ \ 0.3]$ to get the respective value of VSM 1, 2 and 3. For non-uniform inertia and damping, the system has two pole pairs with (depending on the damping) non-zero imaginary part. For uniform ρ, if both pole pairs are non-real, they lie on the same ρ-isoline. For the range of inertias and damping investigated here, oscillations are in the range of 0.1Hz to 10Hz. Fig. 4 shows the 5 poles of the system for $J = 0.46 \times [0.6\ \ 0.4\ \ 0.3]\text{kgm}^2$ and $\rho = 47.11\text{s}^{-1}$ as red marks for the case where $\sigma = 1$ (only VF and no frequency droop is used). In this limit case, one pole is at the origin, two poles are on the real axis and two are on the line $\rho = 47.11\text{s}^{-1}$. The pole in the origin moves along the real axis towards the point $[-47\ \ 0]s^{-1}$ for decreasing σ to zero (colors from orange to dark blue) while the remaining 4 poles do not move. This is because σ correlates inversely with the strength of the coupling of a VSM to the reference frequency ω_n. This

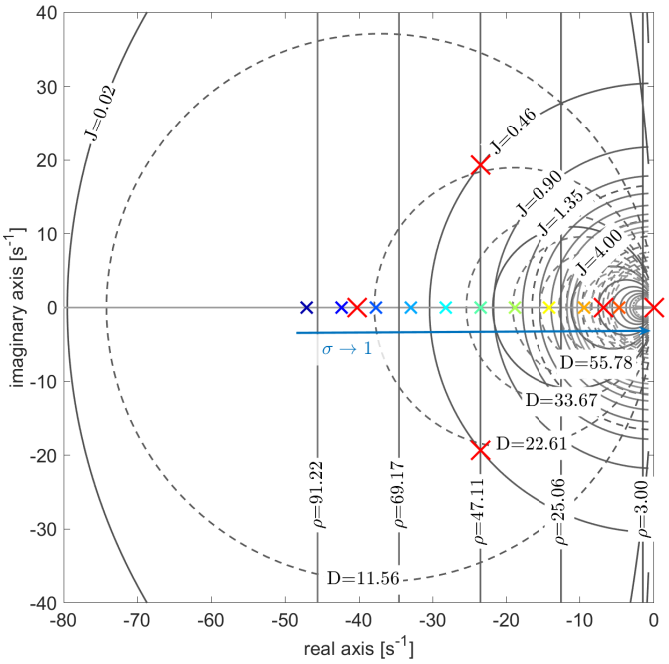

Figure 4: Poles of the linearized NRPS model representing the network from Fig. 6 with data as at the end of this section. There are 5 poles for the 3 VSM systems of which 4 correspond to the angular oscillations and one to the frequency dynamics. The colored marks indicate the pole positions for the model with color changing with increasing $\sigma = [0, 1]$ from blue to red. σ only impacts the position of the pole related to the frequency dynamics, which moves from an initial position at -47 to 0. This effect is expected, as the frequency gets less controlled (the impact of this can be seen in Fig. 5). Isometric lines for inertia, damping coefficient are marked by grey lines, where dashed and full lines indicate the position of each of the two pole pairs. The pole on the real axis moves towards the imaginary axis for increasing σ.

behavior is illustrated in Fig. 5, where ω_3 is plotted subsequent to a disturbance for the same settings. It can be seen that for the limit when $\sigma = 1$ (red), the system frequency continuously increases (the pole at the origin acts as an integrator) and the slope of the graph depends on the power imbalance between the sum of the set powers and the consumed electrical power. Thus σ can be used to adjust the pole position on the negative real axis as desired. For an imposed frequency drop such as arising subsequent to the loss of a generation unit, a lower power increase by the VSM is induced for higher σ, while the damping behavior remains unchanged. Of course, a minimum level of frequency droop should be maintained to not move the pole to the origin and to "loose" the reference frequency.

We point out that the microgrid in this paper has been analyzed also in [19], where the influence of different damping strategies on the region of attraction of the microgrid has been shown. Results suggest that VF (when overall damping is sufficiently high) helps to increase the region of attraction of the system, while high frequency droop, although being beneficial in damping oscillations, does not necessarily improve the robustness of the microgrid.

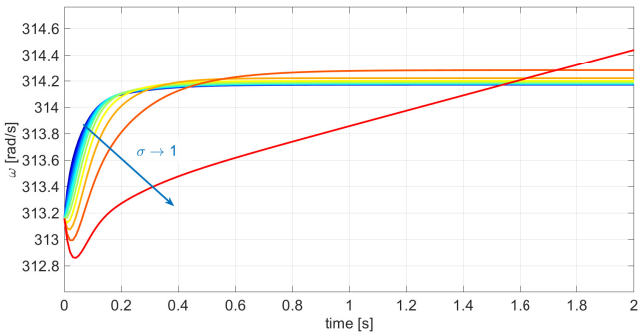

Figure 5: FEPS model: plots for VSM 3 from startup from initial frequency $\omega = 100\pi$rad/s (random initial angles). We show curves for fixed damping ratio $\rho = 47.11\text{s}^{-1}$ and increasing σ from 0 (blue) to 1 (red). When no frequency droop is used (like in the red curve), the model looses a frequency reference and in case of power imbalance acts as an integrator such that $\omega \to \infty$ for $t \to \infty$.

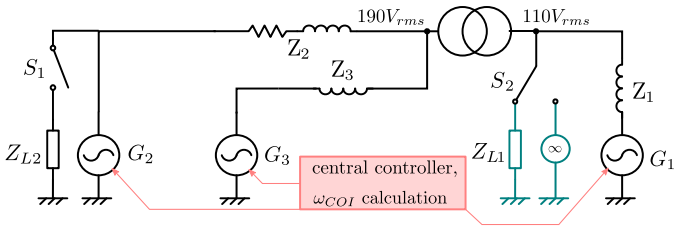

Figure 6: Investigated microgrid of three VSMs, two loads, a transformer and line impedances. S_2 allows either connecting the microgrid to an infinite bus or to a large load L_1. The COI-frequency is calculated in the central controller which receives the VSMs frequencies and sends back ω_{COI} to the inverters.

III. Experimental validation

We show experimental results for a microgrid consisting of three VSMs, line impedances, a transformer and loads. The setup is shown in Figs. 6 and 7. S_2 allows to connect the microgrid to an infinite bus or to a load L_1, both emulated by a programmable AC power supply or to disconnect both. There are two voltage levels in the grid separated through a delta-wye transformer: VSMs G_1 and G_2 are connected on the high voltage (190V_{rms}) side and a third VSM (G_3) is connected at the low voltage side (110V_{rms}). L_2 consists of three line-to-line connected resistors of 110Ω each, representing a 2.95kW load at 190V_{rms}. The line impedances (per line) are $Z_1 = 2\text{mH}$, $Z_2 = 4\Omega$, 5mH, $Z_3 = 0.3\text{mH}$. We compare the damping of oscillations subsequent to a disturbance created by connecting L_2 in the islanded case (Case 1) and by imposing an external frequency drop such as occurring due to a fault in grid connected mode (Case 2). Five different scenarios are compared, see Tab. I: a badly damped case with only minimum damping (LOW), a case using frequency droop (D), a case using high-frequency droop (DHF) and two cases using virtual friction (VF, VFS). The damping coefficient used for each generator in scenario LOW is called $D_{p,base}$. The ratios ρ of $D_{p,base}$ to the respective inertia are the same for each VSM.

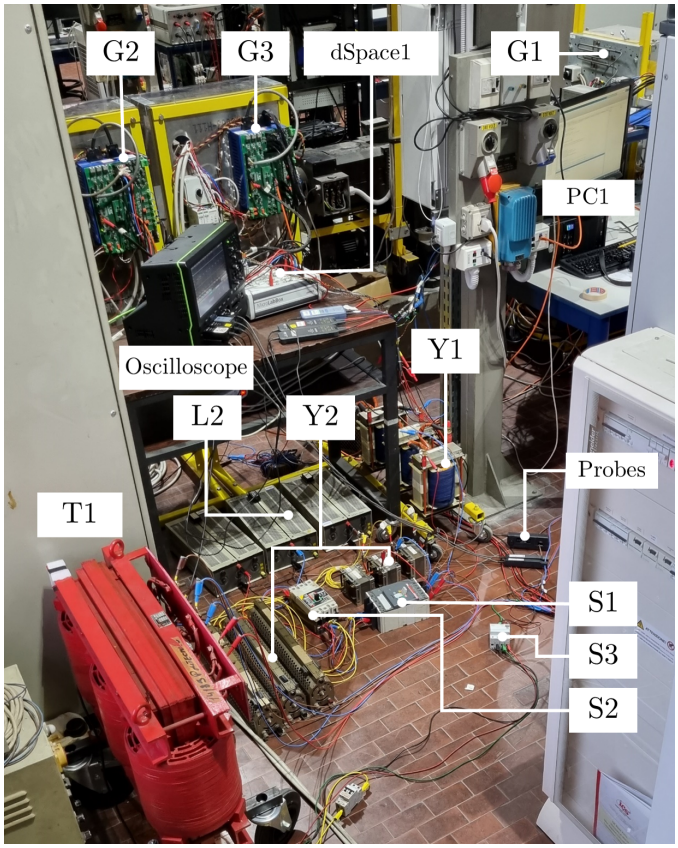

Figure 7: Photo of the experimental setup.

A. Case 1: islanded grid with L_2

In this experiment, the set values were $P_{set} = [3\ 1\ 2]$kW, $Q_{set} = [0.9\ 0.3\ 0.1]$kVar, $J = [0.3\ 0.1\ 0.18]\text{kgm}^2$ and $D_{p,base} = [0.6\ 0.2\ 0.36]\text{kgm}^2/\text{s}$. Fig. 8 shows the change in grounded rotor angle, frequency and output power of G_2 subsequent to the connection of L_2 at $t = 0$s. (The grounded rotor angles are relative rotor angles with respect to VSM 3, see [11]: $\delta_1 = \theta_1 - \theta_3$, $\delta_2 = \theta_2 - \theta_3$.) In scenario LOW, strong oscillations are observed in the grounded rotor angle δ_2, which slowly decay over time. The damping performance in scenarios D, DHF and VF is similar and oscillations only show briefly until up to $t = 1$s. In scenario VFS, oscillations are completely suppressed. All scenarios exhibit the same initial rate of change of frequency (ROCOF), see Fig. 8(b), since the initial decay of the frequency depends on the overall system inertia, which is the same in all scenarios. For scenarios LOW, VF, VFS and DHF, the frequency converges to the same new steady state value. This is due to the fact that the steady state frequency depends on low-frequency droop only. The decay for DHF is slower compared to the other scenarios, since DHF initially strongly acts against a change of frequency, but its effect decays with time. Damping for scenarios LOW, D, DHF and VF is similar, while VFS again shows the strongest damping. The active power output of G_2 in all scenarios shows a peak value of 2kW (Fig. 8c). The sudden increase is due to the inertial response of G_2. The VSM converges to a new

Scenario	D_{LF}	D_{HF}	F	ρ	σ
LOW	1	1	0	2	0
D	5	5	0	10	0
DHF	1	5	0	10	0
VF	1	1	4	10	0.8
VFS	1	1	10	22	0.91

Table I: Investigated scenarios LOW, D, DHF, VF, VFS: the damping coefficients for D_{LF}, D_{HF} and F are obtained by multiplying the base value $D_{p,base}$ with the number shown in the respective cell of this table. The coefficients are such that the overall damping performance is the same for scenarios D, DHF and VF. Scenarios LOW and VFS show lower and higher damping. Note that ρ is defined using D_{HF}.

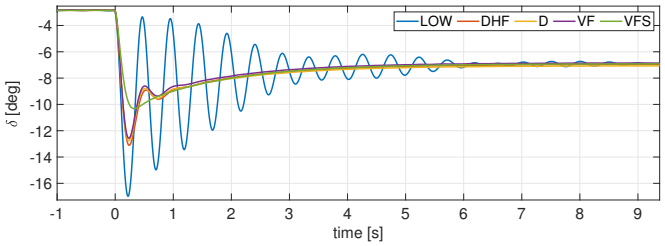

(a) Grounded rotor angles of G_2 w.r.t. G_3.

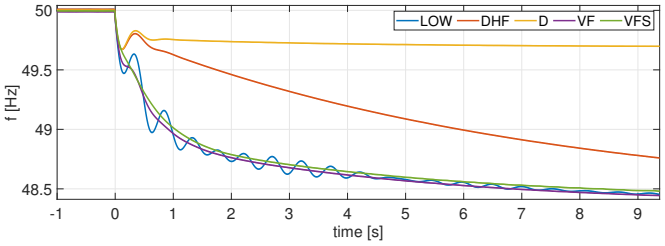

(b) Frequency of G_2.

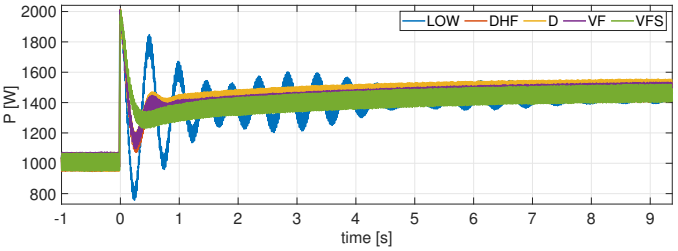

(c) Active output power of G_2.

Figure 8: Load step change by connection of L_2.

steady state of approximately 1.5kW. Here, D, DHF and VF show almost identical damping, while power oscillations occur in scenario LOW.

B. Case 2: grid connected mode

Fig. 9 shows the results for the microgrid connected to a main grid and L_1 disconnected. In this experiment $P_{set} = [3\ 1\ 2]$kW, $Q_{set} = [0.9\ 0.3\ 0.1]$kVar, whereas J and $D_{p,base}$ are the same as before. The main grid imposes a typical frequency drop at $t = 0$s such as observed in a grid comprising synchronous machines, subsequent to the loss of a large generation unit. This frequency drop initially declines to 48.3Hz before it settles at a steady state value of 49.5Hz at about $t = 30$s. The induced oscillations in the grounded rotor angle of G_2 w.r.t. G_3 are strongest in scenario LOW. Maximum angle excursions are best for scenarios VF and

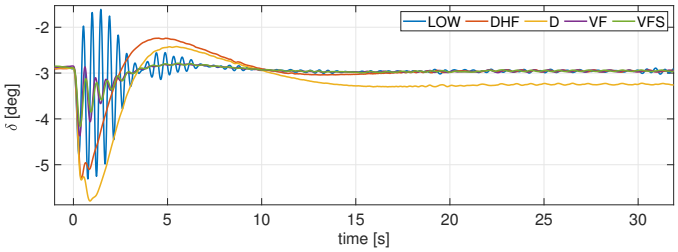

(a) Grounded rotor angles of G_2 w.r.t. G_3.

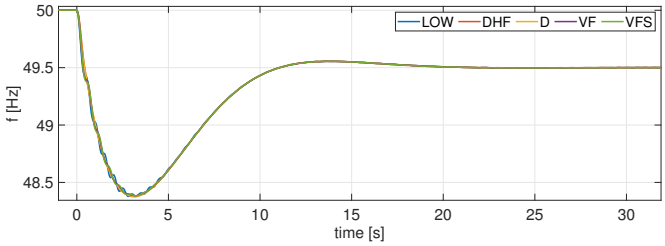

(b) Frequency of G_3.

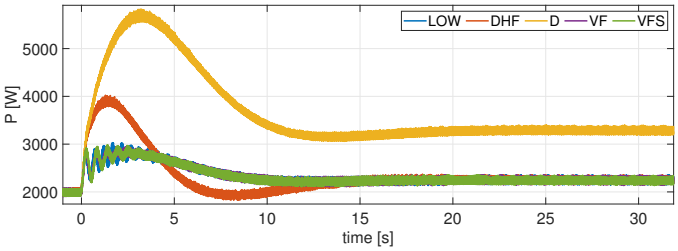

(c) Active output power of G_3.

Figure 9: Frequency drop in grid connected mode.

VFS, but some (damped) oscillations still show compared to scenarios D and DHF. The increase in active power output is largest for scenario D (Fig. 9c). Scenario DHF significantly decreases the active output power during the under frequency and VF and VFS show only minimal increase in output power.

The above data shows that VF is effective in damping oscillations within the microgrid itself, where the frequencies of every machine are known. However, damping with respect to the outside grid cannot be managed with VF alone, if no further damping between the microgrid and the larger grid is imposed. We show in the following how damping with respect to the main grid can be achieved by using stronger HF-droop on one of the VSMs while the other two VSMs operate with low droop. A strong VF damping between all three VSMs ensures the damping between the individual units. In such a case, the stronger damping on VSM 3 is capable of damping the oscillations on VSM 1. In that way, frequency droop can be centralized on one or on some of the units. This allows to allocate grid support features in accordance with the capabilities of the power sources to deliver excess power on demand. Fig. 10 shows data for such an experiment. The plots show the power output of VSM 3 (top) and VSM 1 (bottom) for the already known cases LOW and VF in blue and red, respectively. Then, starting with the yellow curve, the HF-droop coefficient D_{HF} of VSM 3 is increased from 3 to 6. The transient power response of VSM 3 thus strongly increases,

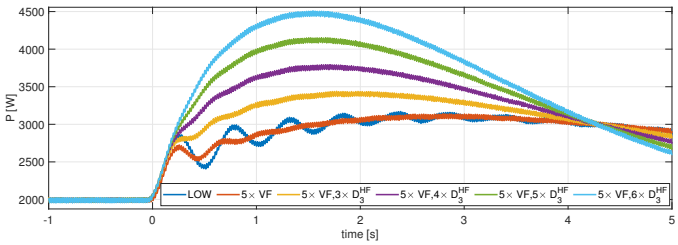

(a) Active output power of G_3.

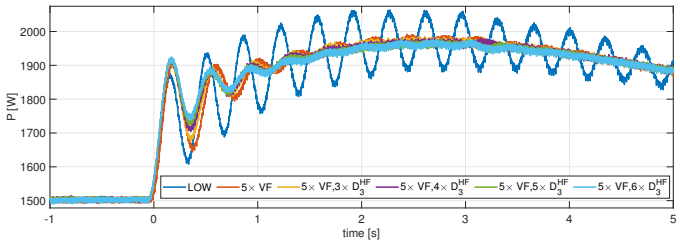

(b) Active output power of G_1.

Figure 10: Active output power of G_1 and G_3 in grid connected mode for different values of HF-droop of G_3.

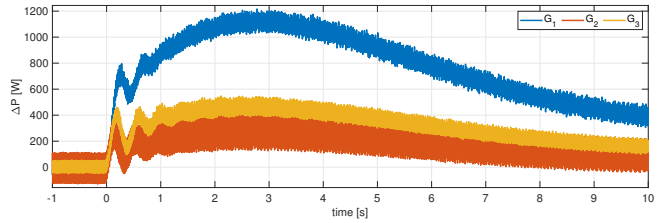

Figure 11: Synchronous oscillations in active output power of the three VSMs.

while the oscillations in VSM 1 decrease. The performance of this method of course depends on the distribution of the inertias J, and notably the generator with higher droop must have a sufficiently large J to impact ω_{COI} in a satisfactory manner.

Finally, Fig. 11 shows the power output of VSM 1-3 for the above experiment with the same damping as the red curve in Fig. 10 (Scenario VF of Tab. I). It can be seen that the power output oscillations of all three VSMs are in phase, which shows the strong damping link between the generators: Indeed, they actually oscillate almost like a single unit against the infinite bus.

IV. Conclusion

This paper provides an experimental validation of VF in a microgrid and have shown that VF allows decoupling frequency support from stability requirements and can be used as an effective damping tool for microgrids ensuring similar damping as frequency droop. For grid connected VSMs, VF can be used to significantly reduce the active power transient response required to achieve a high level of damping between the VSMs. It thus qualifies as an alternative to frequency droop for power sources in a microgrid that cannot afford providing this excess power to ensure stability. We have also shown that VF allows to approach system damping and grid support independently and demonstrates a way to centralize damping, which can be interesting for microgrids where some power sources can offer such services while others are limited.

References

[1] V. Mallemaci, F. Mandrile, S. Rubino, A. Mazza, E. Carpaneto, and R. Bojoi, "A comprehensive comparison of virtual synchronous generators with focus on virtual inertia and frequency regulation," *Electric Power Systems Research*, vol. 201, p. 107516, 2021.

[2] M. Chen, D. Zhou, and F. Blaabjerg, "Modelling, implementation, and assessment of virtual synchronous generator in power systems," *J. of Modern Power Syst. & Clean Energy*, vol. 8, no. 3, pp. 399–411, 2020.

[3] S. Dong and Y. C. Chen, "Adjusting synchronverter dynamic response speed via damping correction loop," *IEEE Transactions on Energy Conversion*, vol. 32, no. 2, pp. 608–619, 2017.

[4] S. Dong, Y. Chi, and Y. Li, "Active voltage feedback control for hybrid multiterminal hvdc system adopting improved synchronverters," *IEEE Transactions on Power Delivery*, vol. 31, no. 2, pp. 445–455, 2016.

[5] Q.-C. Zhong and T. Hornik, *Control of power inverters in renewable energy and smart grid integration*. Wiley, Chichester, UK, 2013.

[6] J. Alipoor, Y. Miura, and T. Ise, "Distributed generation grid integration using virtual synchronous generator with adaptive virtual inertia," in *IEEE Energy Conversion Congress and Exposition*, Denver, CO, 2013, pp. 4546–4552.

[7] Q.-C. Zhong and G. Weiss, "Static synchronous generators for distributed generation and renewable energy," in *2009 IEEE/PES Power Systems Conference and Exposition*, 2009, pp. 1–6.

[8] O. Mo, S. D'Arco, and J. Suul, "Evaluation of virtual synchronous machines with dynamic or quasi-stationary machine models," *IEEE Trans. on Industrial Electronics*, vol. PP, pp. 1–1, 12 2016.

[9] D. B. Rathnayake, M. Akrami, C. Phurailatpam, S. P. Me, S. Hadavi, G. Jayasinghe, S. Zabihi, and B. Bahrani, "Grid forming inverter modeling, control, and applications," *IEEE Access*, vol. 9, pp. 114 781–114 807, 2021.

[10] M. Blau and G. Weiss, "Synchronverters used for damping inter-area oscillations in two-area power systems," in *Int. Conf. on Renew. Energies and Power Quality (ICREPQ)*, Salamanca (Spain), 2018.

[11] F. Reissner, H. Yin, and G. Weiss, "A stability result for network reduced power systems using virtual friction and inertia," *IEEE Transactions on Smart Grid*, vol. 13, no. 3, pp. 1668–1678, 2022.

[12] V. Natarajan and G. Weiss, "Synchronverters with better stability due to virtual inductors, virtual capacitors, and anti-windup," *IEEE Trans. on Industrial Electronics*, vol. 64, no. 7, pp. 5994–6004, 2017.

[13] Z. Kustanovich, S. Shivratri, H. Yin, F. Reissner, and G. Weiss, "Synchronverters with fast current loops," *IEEE Transactions on Industrial Electronics*, 2022, submitted, https://doi.org/10.36227/techrxiv.19887322.v2.

[14] P. Lorenzetti and G. Weiss, "Saturating PI control of stable nonlinear systems using singular perturbations," *IEEE Transactions on Automatic Control*, 2022, early access.

[15] F. Dörfler and F. Bullo, "Synchronization and transient stability in power networks and nonuniform Kuramoto oscillators," *SIAM J. on Control and Optimization*, vol. 50, no. 3, pp. 1616–1642, 2012.

[16] G. Weiss, F. Dörfler, and Y. Levron, "A stability theorem for networks containing synchronous generators," *Systems & Control Letters*, vol. 134, p. 104561, 2019.

[17] H.-D. Chiang, *Direct Methods for Stability Analysis of Electric Power Systems: Theoretical Foundation, BCU Methodologies, and Applications*. Hoboken, NJ: John Wiley & Sons, 2011.

[18] P. Sauer and M. Pai, *Power System Dynamics and Stability*. Stipes Publishing LLC, Champaign, Illinois, 1997.

[19] F. Reissner and G. Weiss, "The region of attraction of a grid with virtual synchronous machines employing virtual friction," in *13th IEEE International Symposium on Power Electronics for Distributed Generation Systems (PEDG)*, Kiel, Germany, 2022.